RSC Advances

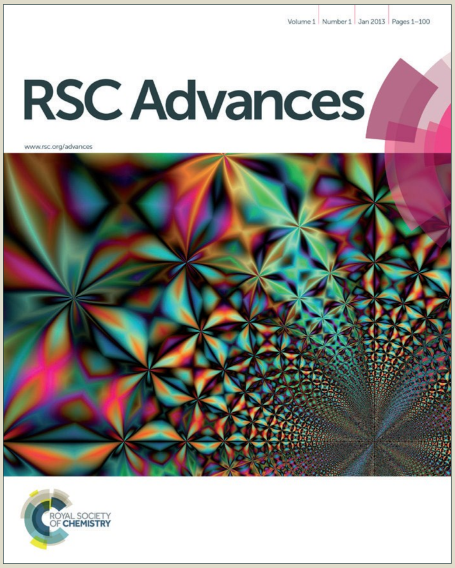

ROYAL SOCIETY OF CHEMISTRY

www.rsc.org/advances

Synthesis of graphene oxide decorated with Core@Double-shell nanoparticles and application for Cr(VI) removal

Binyan Huang[a,b], Yunguo Liu[a,b,]*, Bin Li[c], Guangming Zeng[a,b], Xinjiang Hu[c], Bohong Zheng[d], Tingting Li[a,b], Luhua Jiang[a,b], Xiaofei Tan[a,b], Lu Zhou[a,b].

[a] College of Environmental Science and Engineering, Hunan University, Changsha 410082, P.R. China

[b] Key Laboratory of Environmental Biology and Pollution Control (Hunan University), Ministry of Education, Changsha 410082, P.R. China

[c] College of Natural Resources and Environment, South China Agricultural University, Guangzhou 510642, P.R. China

[d] School of Architecture and Art Central South University, Changsha 410082, P.R. China

*Corresponding author: Yunguo Liu; Tel.: + 86 731 88649208; Fax: + 86 731 88822829;

E-mail address: liuyunguohnu@163.com

Abstract

A novel Graphene oxide composites, namely Fe_3O_4@SiO_2@ Chitosan/GO nanocomposite (MSCG) was synthesized for decontamination of Cr(VI) from aqueous solution. High-resolution transmission electron microscopy revealed a core@double-shell structure of the nanoparticles with iron oxide as the core, silica as the inner shell and chitosan as the outer shell. The characteristic results of Fourier transform infrared (FTIR), scanning electron microscopy (SEM), transmission electron microscopy (TEM), vibrating sample magnetometer (VSM) and X-ray diffraction (XRD) showed that the Fe_3O_4@SiO_2@Chitosan particles were successfully assembled on the surface of the GO layers. The adsorption kinetics followed the pseudo-second-order model and the novel MSCG adsorbent exhibited better Cr(VI) removal efficiency in solutions at low pH. Thermodynamic parameters revealed that the sorption reaction was an endothermic and spontaneous. Moreover, the adsorption capacity was about 90% of the initial saturation adsorption capacity after being used four times. By using a permanent magnet, the recycling process of both the MSCG adsorbents and the adsorbed Cr(VI) is more economically sustainable. These results suggest that MSCG is a potential and suitable candidate for the preconcentration and separation of Cr(VI) from wastewater and for the deep-purification of polluted water.

Keywords: Graphene oxide; Core@Double-shell; Cr(VI); Reduction; Adsorption

1. Introduction

Heavy metal ions contamination is one of the main serious environmental problem in aquatic systems all over the world. Among these heavy metal species, Cr(VI) is a commonly identified contaminant because of its high toxicity, carcinogenicity, mutagenicity and a wider range of applications in industries, whereas Cr(III) is less toxic and can be readily precipitated out from wastewater in the form of $Cr(OH)_3$ [1], therefore, the reduction of Cr(VI) to Cr(III) is deemed as a key process. Since the Cr(VI) is unbiodegradable and apt to accumulate in living tissues, it is particularly dangerous and troublesome, and becoming concentrated throughout the food chain [2]. Its presence is due to a combination of natural processes (volcanic action, erosion of mercury-containing sediments) and anthropogenic activities (industrial effluents of tannery, dyeing, metal plating industries) [3]. The USEPA suggested a 0.1 mg/L permissible limit of the total chromium in drinking water [4]. Recently, the State of California established a Cr(VI) maximum level of 10 μg/L, indicating the tendency for a similar re-evaluation of regulation limits around the world in the near future [5]. Therefore, the removal of Cr(VI) from wastewater is considered to be of urgency before being discharged into aquatic systems. The demand for a simple and cost-effective method for the removal of Cr(VI) is expected to open a wide field for the development of novel adsorbents [6].Conventional Cr(VI) removal techniques including membrane separation, ion exchange, electrochemical reduction/precipitation, reverse osmosis, filtration and adsorption based on various mechanisms [7]. Most of these methods are effective but suffering from disadvantages such as high operational cost and/or large quantity of chemicals. However, adsorption is recognized as one of the most effective and economical treatment methods in wastewater treatment because of its significant advantages including availability, non-hazardous operation, high-efficiency and low-cost materials in comparison with other conventional methods [8].

Chitosan (CS), the linear and partly acetylated (1-4)-2-amino-2-deoxy-β-D-glucan, is a deacetylated product of chitin (found in abundance in nature) [9, 10]. Chitosan is a multifunctional polymer that has a large number of hydroxyl and amino groups, which can be regarded as adsorption sites for metals and have been extensively used as an adsorbent for Cr(VI) [11-15]. In addition, chitosan presents high biodegradability, biocompatibility and low-toxicity [16-18].However, despite the numerous advantages and unique properties of chitosan, its use in a wider range of applications is restricted by its poor mechanical and electrical properties [19]. An effective method for improving the physical and mechanical properties of CS is to form organic–inorganic composites through incorporation of nanofillers, such as metal nanoparticles, clays, carbon nanotubes and graphene oxide [20].

Graphene, a member of carbon-based nanomaterials with a lamellar structure, due to its sp^2 hybrid carbon network as well as extraordinary mechanical, electronic, thermal properties and a high theoretical surface area [20, 21], recently was attracted intense interest for its potential application as adsorbent material [22]. Graphene oxide(GO) can be synthesized after graphite oxidation with strong oxidizing agents such as potassium permanganate, which makes GO have a number of oxygen functional groups, such as -OH, -COOH, -O-, and C=O, covalently attached to its layers [23]. These oxygen hydrophilic functionalities make GO dispersible in water as well as some organic solvents extensively, and easier to intercalate [24, 25]. Intercalation of CS into GO could enhance the physical and chemical properties derived synergistically from both components. Recently, chitosan/graphene oxide nano composites have been concerned by the crosslinking agent, such as glutaraldehyde [26, 27].

Since this composite material is preferably soluble in water, separation is difficult. As compared with the conventional methods (filtration or centrifugation), magnetic separation requires less energy and result to better separation by the action of an external magnetic field [22, 28-30]. For example, Li et al. fabricated magnetic cyclodextrin–chitosan/graphene oxide (CCGO) with a saturation magnetization of 22.15 emu/g for Cr(VI) removal and the maximum sorption capacity was 67.66 mg /g [21]. Zhu et al. reported a one-pot synthesis of magnetic graphene nanocomposites decorated with core@double-shell nanoparticles as the sorbent for Cr(VI) pollutant [31]. However, there are two major challenges. One is related to the reunion, poor dispersion of Fe_3O_4 in water. The other is the easy oxidation/dissolution of iron nanoparticles, especially at high concentrations of acid solution [32]. To solve these problems, a suitable shell structure or decorative material of $Fe_3O_4@SiO_2$ is often introduced [33-36], and the silica shell is convenient for the material to be grafted onto chitosan, which can also make the core-shell structure more stable [37].

The objective of this paper focused on enhancing the Cr(VI) removal ability by the Graphene oxide composites, namely Fe_3O_4@SiO_2@Chitosan/GO nanocomposite (MSCG). The samples were characterized by SEM, TEM, FTIR, XRD, XPS, VSM and zeta potential. In addition, we have conducted kinetic, isothermal and thermodynamic analysis. The Cr(VI) removal mechanisms was investigated by XPS analysis. The results show that such superparamagnetic particles are efficient support for the adsorption and repeated use.

2. Materials and Methods

2.1 Materials

Chitosan (95% degree of deacetylation) was commercially available from Macklin Biochemical Co., Ltd. (Shanghai,China). $FeCl_3 \cdot 6H_2O$ (AR), $K_2Cr_2O_7$ (GR), polyethylene glycol (PEG) 2000 (CP), ethylsilicate (TEOS), glutaraldehyde solution (BR) and all other chemicals used in this study were purchased from Sinopharm Chemical Reagent Co., Ltd. (Shanghai,China), all of which were analytical grade and used without further purification. In this paper, double deionized water was used in the preparation of all solutions.

2.2 Preparation of Fe_3O_4@SiO_2

1.35 g of $FeCl_3 \cdot 6H_2O$ were dissolved in 40 mL of ethylene glycol to form a clear solution, and 1.0 g of PEG2000 and 3.6 g of sodium acetate were added immediately under stirring until they were completely dissolved. Then the mixture was transferred into a Teflon lined stainless steel autoclave, and maintained at 473 K for 8 h, and then allowed to cool to room temperature. Finally the resulting products (Fe_3O_4 particles) were collected by magnetic separation, washed several times by water and alcohol respectively. And dried in the vacuum oven at 323 K.

The core/shell structured Fe_3O_4@SiO_2 microspheres were synthesized through a modified Stöber method [38]. 0.1 g of the as-prepared Fe_3O_4 particles were dispersed in a mixture of 100 mL ethanol, 25 mL water, and 1.5 mL $NH_3 \cdot H_2O$ with the help of ultrasonication. Afterward, 1 mL TEOS was added dropwise and the reaction was allowed to proceed for 6 h under stirring. The obtained product was collected by magnetic separation and rinsed with distilled water and ethanol several times, and then dried under vacuum at 333 K.

2.3 Preparation of GO

GO was prepared by purified natural graphite powder following the modified Hummers method reported in the literature [39]. Briefly, 2.0 g graphite and 1 g $NaNO_3$ were placed in a 250 mL beaker. Then, 46 mL of sulfuric acid (98%) was added with stirring in ice bath. While maintaining the temperature below 283 K, 6 g $KMnO_4$ and 1 g $NaNO_3$ were slowly added to the suspension with vigorous stirring. After stirred for 2 h in ice bath, the mixture was stirred at 303 K for 30 min. Next, the paste was diluted with 92 mL double deionized water under vigorous agitation, heated to 368 K and then maintained for 30 min. When the suspension was allowed to cooled to 333 K, 10 mL H_2O_2 (30 wt.%) solution was added to the mixture to terminate the reaction and the mixture was stirred for 2 h at room temperature. After centrifugation, the precipitate was washed repeatedly with 5% HCl to remove residual metal ions, and then with double deionized water to remove the sulfate ion. Finally, the precipitate (graphene oxide) was bath sonicated and dried under vacuumat 338 K.

2.4 Preparation of Fe_3O_4@SiO_2@ Chitosan/GO(MSCG)

The preparation process of MSCG was as follows: 0.4 g pure chitosan was dissolved in 20 mL of acetic solution (2% v/v), and the mixture was sonicated for 30 min. Subsequently, 0.16 g of magnetic particles (Fe_3O_4@SiO_2) was added into the colloidal solution and the reaction system was continued to be stirred for 1.5 h. Next, 3 mL of glutaraldehyde was added to crosslink chitosan. Then, 0.3 g of GO was added and the pH of the reaction system was adjusted to 9-10. Finally, the mixture was kept in a water bath for a further 60 min at 353 K. The precipitate were washed with ethanol and distilled water in turn until pH was about 7 and was dried in a vacuum oven at 323 K. The fabrication procedure of the MSCG composite is schematically depicted in Scheme 1.

2.5 Characterizations of MSCG

The surface morphologies of adsorption materials were observed by the field emission scanning electron microscope (SEM, Hitachi S-4800, Japan) and transmission electron microscopy (TEM, Tencnai G2 F20, USA). Fourier transform infrared spectrum (FTIR) measurements were carried out by using Nicolet Magna-IR 750 Spectrometer at room temperature. Wide angle X-ray diffraction (XRD) patterns were recorded by a D8 ADVANCE X-ray diffraction spectrometer (Bruker, German). Zeta potential of the composite was measured using a Zeta-sizer Nano-ZS (Malvern, UK). The surface chemical compositions of MSCG were analyzed based on the XPS spectra (Thermo Fisher Scientific, UK) .

2.6 Sorption experiments

All batch adsorption experiments of Cr(VI) were carried out by using the MSCG as the adsorbent in 50 mL Erlenmeyer flask with a shaking speed of 160 rpm. The stock solution (1000 mg/L) of Cr(VI) was prepared by dissolving 2.829 g $K_2Cr_2O_7$ in 1000 mL double deionized water in a volumetric flask. Typically, a 50 mL solution of known Cr(VI) concentration and 0.02 g of MSCG were added into 100 mL glass flasks and then shook under 298 K. The pH was adjusted to desired values by adding negligible volumes of NaOH or HCl. After being mixed for 24 h, the mixture was drawn and separated immediately by the aid of a permanent magnet. Residual Cr(VI) concentration in supernatant was measured using a UV spectrophotometer (UV-2550, SHIMADZU, Japan) at 540 nm according to the National Standard of the People's Republic of China. The amount of Cr(VI) adsorbed onto MSCG at equilibrium was calculated using the following equation:

$$\mathrm{q}_e = \frac{C_\mathrm{o} - C_e}{m} V \quad (1)$$

where q_e is the adsorption quantity (mg/g); C_o and C_e is the initial and equilibrium concentrations of Cr(VI) in solution (mg/L), respectively; V is the volume of solution (L), and m is the weight of MSCG (g).

All experiments were duplicated, and only the average values were reported. The maximum errors were less than 5%.

3. Results and discussion

3.1. Characterization of MSCG

Fig. 1 showed the magnification images of Fe_3O_4, Fe_3O_4@SiO_2, GO, MSCG. As shown in Fig.1a, the average size of Fe_3O_4 is about 250 nm, and the roughness of the nanoparticles surface can be discerned clearly (Fig. 1a). After being coated with a silica layer, the typical core–shell structure of the Fe_3O_4@SiO_2 can be observed, the surface becomed smoothly and the average size increased to about 400 nm (Fig. 1b). Fig. 1c and Fig. 1e showed a typical SEM and TEM image of GO, which presented a sheetlike structure with large thickness, smooth surface, and wrinkled edge. After combination with Fe_3O_4@SiO_2 and chitosan to form the MSCG composite (Fig. 1d), the MSCG had a much rougher surface, which revealed that many small Fe_3O_4@SiO_2@Chitosan particles had been assembled on the surface of the GO layers with a high density, and the construction of the Fe_3O_4@SiO_2@Chitosan was Core@Double-shell with iron oxide as the core, silica as the inner shell and chitosan as the outer shell (Fig. 1f). Meantime, the average diameter less than 1 μm as estimated from the SEM image.

The XRD patterns of Fe_3O_4, Fe_3O_4@SiO_2 and MSCG were shown in Fig. 2, indicating the presence of magnetite particles (Fe_3O_4). The six characteristic peaks of Fe_3O_4 at 2θ = 30.1°, 35.5°, 43.2°, 53.6°, 57.1°, and 62.7°, corresponding to the indices (220), (311), (400), (422), (511) and (440), respectively, were observed in both samples. These indexed peaks of Fe_3O_4 using the Joint Committee on Power Diffraction Standards database (JCPDS 19-0629) with a cubic inverse spinel structure

[40], which is ascribed to the strong signals of the iron oxides. It is indicated that the multiple composite has been successfully prepared and the phase structure of each component has no change.

The FTIR spectra of Fe_3O_4, Fe_3O_4@SiO_2, GO and MSCG were shown in Fig. 3. The characteristic sorption band of Fe_3O_4 at 580 cm^{-1} was attributed to the stretching vibration of Fe-O bond. For Fe_3O_4@SiO_2, apart from the peak at 580 cm^{-1}, the strong peak at 1120 cm^{-1} resulted from Si-O vibrations, which confirmed the successful coating of silica layers on Fe_3O_4 [41]. As for the GO, several characteristic FTIR peaks were observed, for examples, C-O-C (1050cm^{-1}), C-OH (1384cm^{-1}), C=C (1627cm^{-1}), C=O (1730cm^{-1}), O-H (3420cm^{-1}). Similarly, in the FTIR spectra of MSCG, the same functional groups above mentioned were found around the corresponding wavenumber. However, the peak at 1730 cm^{-1}, which can be attributed to carboxyl groups, disappeared for MSCG. The characteristic bands appeared at 1639 cm^{-1} ascribed to the amide I (C=O stretching), at 1596 cm^{-1} ascribed to amide II (N-H blending modes), confirming that the carboxyl groups reacted with chitosan during the preparation of the composite. The broad peak responsible for vibrational frequency of -OH group was decreased in case of MSCG than GO, which implied that the -OH groups were also taking part in hydrogen bonding with the chitosan molecule. Thus, it can be concluded that Core@Double-shell has been grafted successfully to the GO surface.

XPS analysis was performed on MSCG before and after its adsorption on Cr(VI). The full scan XPS spectrums before adsorption (Fig. 4a) showed the presence of C, N and O element at the binding energy of 285.19 eV, 399.2 eV and 532.2 eV. As shown in Fig. 4b, the C1s band of MSCG can be deconvoluted into four peaks centered at 284.6, 285.7, 286.4 and 287.8 eV, corresponding to the C=C/C-C, C-N, C-O and C=O respectively. The N1s band of MSCG (Fig. 4c) can be deconvoluted into three peaks, corresponding to -N= (398.7 eV), -NH- (399.5 eV) and positively charged nitrogens N^+ (402.3 eV). The high-resolution O1s spectra of the samples (Fig. 4d) were curve-fitted by three peaks: the first peak at 530.8 eV attributed to Fe-O (Fe_3O_4), the second at 532.4 eV due to O-H groups, and the third at 533.3 relevant to O-C-O moieties (epoxy, carboxy groups) [40]. These results are agreed with characterization by FTIR.

The room-temperature magnetization hysteresis loops of Fe_3O_4, Fe_3O_4@SiO_2 and MSCG was measured using vibrating sample magnetometry (VSM) to study the magnetic properties. As can be seen in Fig. 5. The saturation magnetization is found to be 74.0, 67.0 and 10.5 emu/g for Fe_3O_4, Fe_3O_4@SiO_2 and MSCG, respectively. This decline can be attributed to the relatively low amount of Fe_3O_4, the existence of GO and the surface modification by CS [42]. Although the saturation magnetization values of MSCG are lower than that of bare Fe_3O_4 and Fe_3O_4@SiO_2, the magnetic propertyof MSCG remained high enough to meet the needs for magnetic separation. This simple magnetic separation experiment proved that the magnetic property of MSCG provided an efficient way to separate MSCG easily from the solution with the help of an external magnetic force, which is essentially important for the convenient recycling of the MSCG composite. This figure also showed almost zero coercivity and remanence, which indicated the super-paramagnetic properties of the synthesized magnetic nanoparticles. Super-paramagnetic particles can respond to an external magnetic field without retaining any magnetism after removal of the applied magnetic field. This feature allowed those nanoparticles for highly efficient magnetic manipulation when used as nano-adsorbents for removal of Cr(VI) from aqueous solution under relatively low external magnetic field.[43]

3.2 Effect of pH

The pH value has been identified as the most important fator by changing the surface charge of the adsorbent and also the speciation distribution of heavy metals in solution phase. As shown in Fig.6, the pH effects on the adsorption of Fe_3O_4, $Fe_3O_4@SiO_2$ and MSCG have been studied at pH 1-10 and 298 K. The results demonstrate that the adsorption ability of Fe_3O_4 and $Fe_3O_4@SiO_2$ were much lower compared with the MSCG,and the values of q_e were less than 20 mg/g. However, the maximum adsorption of Cr(VI) on the MSCG surface was 145 mg/g at pH 2, and the adsorption capacity was gradually reduced as the pH increased. This result can be interpreted as follows. In aqueous environment, Cr(VI) exists in five main forms, including $Cr_2O_7^{2-}$, $HCr_2O_7^-$, CrO_4^{2-}, $HCrO_4^-$ and H_2CrO_4. These ion forms are related to the solution pH and total chromate concentration [44]. CrO_4^{2-} is predominant when pH > 6.0, while $Cr_2O_7^{2-}$ or $HCrO_4^-$ are the main species at pH 2.0–6.0 and H_2CrO_4 is primary at pH < 1.0 [45].The high adsorption efficiency at low pH can be attributed to the fact that the surface of the adsorbent becomes highly protonated and positively charged, which favors the uptake of Cr(VI) anions through electrostatic attraction.

While MSCG has the nitrogen species, which can be protonated to positively charged nitrogens in acidic conditions, and they could absorb negatively charged $HCrO_4^-$ or $Cr_2O_7^{2-}$ through electrostatic attraction. Meanwhile, low pH also promoted the redox reactions in the aqueous and solid phases, because the protons could participate in the following reaction as follows [21]:

$$HCrO_4^- + 7H^+ + 3e \rightarrow Cr^{3+} + 4H_2O \qquad (2)$$

During the adsorption, Cr(VI) was partially reduced to Cr(III) by the reductive surface nitrogen species on the MSCG. The resulting Cr(III) precipitated on the surface of the MSCG in the form of Cr_2O_3 [46]. With the increase of pH, the uptake of Cr(VI) decreased, which was due to the higher concentration of OH^- ions present in the mixture that compete with Cr(VI) species. These results agreed with the zeta potential of MSCG which was shown in Fig. 7. The pH of point of zero charge (pH_{ZPC}) of MSCG estimated by zeta potential was 3-4. When the pH was 3-4, zeta potential shift from positive to negative with the major driving force from electrostatic force to electrostatic repulsion, so as to the adsorption efficiency decreased significantly compared to the slowly decreases at pH > 4. Whereas highly acidic conditions (pH 1) were not favorable because of the competition between protons and anionic metallic species ($HCrO_4^-$) , which explained the weak adsorption.

3.3. Adsorption kinetics

For the purpose of investigation and comparison of the rate-controlling step in the adsorption mechanism, the kinetic data were dealt with pseudo-first order, pseudo-second order and intra-particle diffusion models at three different initial Cr(VI) concentrations (100, 150, 200 mg/L) in this study. The best-fit model was selected based on the correlation coefficient (R^2) values of the linear regression.

The pseudo-first order model is described in the following equation:

$$\ln(q_e - q_t) = \ln q_e - k_1 t \qquad (3)$$

Another kinetic model is pseudo-second-order, which is expressed by:

$$\frac{t}{q_t} = \frac{1}{k_2 q_e^2} + \frac{t}{q_e} \qquad (4)$$

where q_e (mg/g) and q_t (mg/g) represent the adsorption capacity at equilibrium and at time t, k_1 (min^{-1}) is the the rate constant of pseudo-first order adsorption, while k_2 (g/mg·min) is the rate constant of pseudo-second order model.

The kinetic parameters are presented in Table 1 and the plots of pseudo-second-order kinetic model are shown in Fig.8a. The values of q_e and k_2 can be determined by the slope and intercept of the straight line of the plot t/q_t versus t, respectively. As can be seen, the values of the correlation coefficients indicated a better fit of the pseudo-second order model with the experimental data compared to the pseudo-first order, since all of its correlation coefficient (R^2) values are beyond 0.997, which were higher than that of the pseudo-first order model (below 0.983). In addition, the calculated q_e values were very close to the theoretical ones, which suggested that the dominant rate-limiting step of the adsorption mechanism might be due to chemical adsorption, high specific surface area and the absence of internal diffusion resistance [43].

In order to identify the possible rate controlling procedure that affected the kinetics of adsorption, intra-particle diffusion model was further examined. The rate parameter for intra-particle diffusion was determined by the following equation:

$$q_t = k_i t^{1/2} + C \qquad (5)$$

Where k_i is the intra-particle diffusion rate constant (mg/g min$^{1/2}$), and C_i is the intercept related to the thickness of the boundary layer.

According to this model, if the regression of q_e vs $t^{1/2}$ is linear and passes through the origin, then the sole rate-limiting step is intra-particle diffusion, otherwise not [47]. As shown in Fig.8b. the plotting of q_t vs $t^{1/2}$, multi-linear including three linear sections, it could be seen that the intra-particle diffusion was not the only rate-limiting step, other processes might also be involved. The first section of the curve with a large slope may be attributed to the film diffusion, corresponding to the transportion of Cr(VI) from the bulk solution to the external surface of MSCG. The second portions are the gradual sorption stage, which corresponds to the diffusion of the Cr(VI) from the external surface into the pores of the MSCG. The final linear portions indicate the final equilibrium stages where the intra-particle diffusion starts to slow down. The model parameters obtained from the sections of plots are listed in Table 2. Therefore, both film diffusion and intra-particle diffusion occur simultaneously, and the intra-particle diffusion is not the only rate controlling step for the whole process [48].

3.4. Sorption isotherms and thermodynamics

In general, two isotherm models are available to describe the equilibrium sorption distribution, namely Langmuir and Freundlich isotherms. The Freundlich isotherm is an empirical equation employed to describe heterogeneous systems, while the Langmuir adsorption isotherm assumes a homogeneous adsorption process [47]. The nonlinear equations of Langmuir and Freundlich sorption isotherms were used to fit the Cr(VI) adsorption process on MSCG at 298, 308 and 318 K, as shown in Fig.9.

The mathematical expression of the Langmuir model is

$$q_e = \frac{q_{\max} K_L C_e}{1 + K_L C_e} \tag{6}$$

where $q_{\max}$ is the ultimate adsorption capacity (mg/g), C_e is the equilibrium concentration of sorbent in solution (mg/L), q_e is the equilibrium loading of sorbate on sorbant (mg/g), and K_L is the relative energy of adsorption (L/mg).

The Freundlich model is expressed as

$$q_e = K_F C_e^{1/n} \tag{7}$$

where K_F and n are Freundlich isotherm constants related to adsorption intensity of the adsorption capacity and adsorbent, respectively.

The values for the Langmuir and Freundlich constant and correlation coefficients (R^2) are calculated and shown in Table 3. From the correlation coefficients (R^2) and the fitting curves (Fig.9), we can see that the Freundlich model fitted the experimental data better than the Langmuir model, indicating that the adsorption did not follow monolayer adsorption. The 1/n values are far less than 1, implying that favorable adsorption was for Cr(VI) onto MSCG at all temperatures studied. Therefore, the uptake of Cr(VI) preferably followed multilayer and heterogeneous adsorption processes.

In order to provide in-depth information about internal energy changes associated with sorption, the thermodynamic parameters such as change in Gibbs free energy (ΔG^o), enthalpy (ΔH^o) and entropy (ΔS^o) at three different temperatures were estimated to evaluate the feasibility and nature of the adsorption reaction. The Gibbs free energy change of the process is related to the equilibrium constant (K_c = $1000q_e/c_e$) by the following equation：

$$\Delta G^o = -RT\ln\left(K_c\right) \tag{8}$$

According to thermodynamics, the Gibbs free energy change is also related to enthalpy change and entropy change at constant temperature by the following equation：

$$\Delta G^o = \Delta H^o + T\Delta S^o \tag{9}$$

From eqs 8−9, one can write:

$$\ln\left(K_c\right) = \left(-\frac{\Delta H^o}{R}\right)\frac{1}{T} + \frac{\Delta S^o}{R} \tag{10}$$

The values of △H° and ΔS° were calculated from the slope and intercept of the linear plots of ΔG° versus T. The slope and intercept of the plot give the ΔS° and the ΔH° values, respectively. The values obtained are given in Table 4. According to Table 4, the decrease of negative values of ΔG^o with the increase of temperature from 298 to 318K revealed that the adsorption process was more favourable at higher temperatures. Based on thermodynamic theory, the negative values of ΔG^o suggest that the process was spontaneous with high preference for Cr(VI). Furthermore, the positive values of ΔS^o emphasized the increased randomness at the interface of solid/solution interface with possible micro-structural changes of the adsorbate and adsorbent [22], and the positive values of ΔH^o suggest the endothermic nature of the adsorption in the process. Because the adsorption was endothermic, the amount adsorbed at equilibrium was increased with increasing temperature. The results imply that the sorption of Cr(VI) on MSCG is an endothermic and spontaneous process.

3.5 Removal mechanism .

To investigate the mechanism of Cr(VI) removal, XPS analysis has been carried out and the wide XPS spectra of the MSCG composite after Cr(VI) adsorption was given in Fig.10a. After Cr adsorption, typical Cr XPS peak appeared. The deconvolution of Cr 2p XPS peak were divided into the peak at 586.9 eV for Cr(VI) and the peak at 577.3 eV for Cr(III), respectively [4]. Thus, it can be inferred that both Cr(III) and Cr(VI) are simultaneously existing on the surface of the MSCG composite after adsorption process. The existence of Cr(VI) species was mainly due to the adsorption of Cr(VI) through the electrostatic interaction. However, the presence of Cr(III) on the surface of MSCG originated from the chemical reduction interaction. Based on the above analyses and discussion, the Cr adsorption mechanism was illustrated in Scheme 2. The Cr adsorption involved (i) the rapid diffusion of Cr(VI) to the surface of MSCG and the Cr(VI) adsorption on protonated and positively charged nitrogens on MSCG, (ii) the relatively retarded diffusion of Cr(VI) to inner pore and simultaneous transformation of Cr(VI) to less toxic Cr(III) by the reduction of nitrogen species [47], followed by Cr(III) chelated on -NH- groups.

In addition, the nitrogen species of MSCG played crucial important roles in the reduction process of MSCG-metal interface [4]. To verify this speculation, the N 1 s XPS spectrum of MSCG composite before and after adsorption is shown in Fig. 10b. For MSCG, N 1s peak was deconvoluted into three peaks, 9.2% of -N= at 398.7 eV, 74.0% of -NH- at 399.5 eV and 16.8% of positively charged nitrogens (N^+) at 402.3 eV. The presence of N^+ could absorb negatively charged $HCrO_4^-$ through electrostatic attraction in acidic conditions.Meanwhile, low pH also promotes the redox reactions in the aqueous and solid phases, leading to the Cr(VI) reduced to Cr(III) via spontaneous electron comes from nitrogen species, and the -N=, -NH- unites produced positively charged nitrogens N^+. As can be seen from Fig. 10b, after Cr(VI) adsorption, the molar ratio of N^+ increased significantly from 16.8% to 33.4% , the -N= disappeared and -NH- decreased from74.0% to 66.6%. As the Cr(III) chelated on -NH- groups, leading to the accumulations on the MSCG surface, the overall adsorption process between the MSCG and the Cr(VI) is finally reached equilibrium.

3.6 Regeneration of saturated adsorbents

From practical point of view, the recyclability is an important factor for evaluating the economy and applicability of adsorbents. Such adsorbent has higher adsorption capability as well as better desorption property which will reduce the overall cost for the adsorbent [49]. To investigate the reusability, the MSCG was soaked in 0.1 M NaOH for 5 hours after one adsorption and reintroduced into a fresh Cr(VI) solution (pH=2) for another cycle at 298 K. The reusability of MSCG was shown in Fig.11. Because of the magnetic properties, the collection of Cr(VI)-adsorbed MSCG was very easy and fast. It can be seen from Fig.11 that only a slight loss in adsorption capacity after four consecutive cycles of adsorption-desorption, in the meantime, the adsorption capacity remained at 90% after four cycles and after that it decreased rapidly. The decrease of activity can be considered as two reasons: (1) Cr(VI) adsorbed on MSCG cannot be completely desorbed from the cavities of the chitosan, (2) because of the nitrogen species on the surface of MSCG, Cr(VI) was partially reduced to Cr(III). At lower pH, some Cr(III) was precipitated on the surface of the MSCG in the form of Cr_2O_3 [46]. The availability of the active sites would decrease with the increase in Cr_2O_3 remaining on the MSCG. Thus leading to less Cr(VI) to be adsorbed by the used MSCG. These results show that the adsorbents can be recycled for Cr(VI) adsorption, and the adsorbents can be reused.

4. Conclusions

A novel graphene-based adsorbent (MSCG) was successfully prepared via a simple chemical synthesis method. The MSCG exhibited superparamagnetic behavior at room temperature and could be separated by an external magnetic field. The sorption kinetics studies illustrated that the kinetics data could be well described with pseudo-second-order model and the intra-particle diffusion was not the only rate-limiting step. The equilibrium data were fitted the Freundlich model better than the Langmuir model. The sorption reaction was an endothermic and spontaneous process. Decontamination of Cr(VI) was found to be more effective in the lower pH range and at higher temperatures. Cr(VI) removal in aqueous solution did not only include the electrostatic attraction on the composite surface, but also involved the reduction process from the Cr(VI) to the low-toxic Cr(III). This research indicates that MSCG is an effective and potential sorbent for Cr(VI) removal from wastewater.

Acknowledgments

The study was financially supported by the National Natural Science Foundation of China (Grant no. 41271332 and 51478470) and the Science and Technology Planning Project of Hunan Province, China (Grant No. 2012SK2021).

References

1. X. Mo, Z. H. Yang, H. Y. Xu, G. M. Zeng, J. Huang, X. Yang, P. P. Song and L. K. Wang, *J. Hazard Mater.*, 2015, **286**, 493-502.
2. S. C. Xu, S. S. Pan, Y. Xu, Y. Y. Luo, Y. X. Zhang and G. H. Li, *J. Hazard Mater.*, 2015, **283**, 7-13.
3. L. Wu, L. Liao, G. Lv and F. Qin, *J. Contam. Hydrol.*, 2015, **179**, 1-9.
4. H. Wang, X. Yuan, Y. Wu, X. Chen, L. Leng, H. Wang, H. Li and G. Zeng, *Chem. Eng. J.*, 2015, **262**, 597-606.
5. C. E. P. Agency, 2014.
6. K. Simeonidis, E. Kaprara, T. Samaras, M. Angelakeris, N. Pliatsikas, G. Vourlias, M. Mitrakas and N. Andritsos, *Sci. Total. Environ.*, 2015, **535**, 61-68.
7. A. G. Tekerlekopoulou, M. Tsiflikiotou, L. Akritidou, A. Viennas, G. Tsiamis, S. Pavlou, K. Bourtzis and D. V. Vayenas, *Water Res.*, 2013, **47**, 623-636.
8. A. Kara, E. Demirbel, N. Tekin, B. Osman and N. Besirli, *J. Hazard Mater.*, 2015, **286**, 612-623.
9. R. A. A. Muzzarelli, J. Boudrant, D. Meyer, N. Manno, M. DeMarchis and M. G. Paoletti, *Carbohyd. Polym.*, 2012, **87**, 995-1012.
10. A. A. Azeez, K. Y. Rhee, S. J. Park, H. J. Kim and D. H. Jung, *Compos. Part B-Eng.*, 2013, **50**, 127-134.
11. C. Jung, J. Heo, J. Han, N. Her, S.-J. Lee, J. Oh, J. Ryu and Y. Yoon, *Sep. Purif. Technol.*, 2013, **106**, 63-71.
12. L. Sun, Z. Yuan, W. Gong, L. Zhang, Z. Xu, G. Su and D. Han, *Appl. Surf. Sci.*, 2015, **328**, 606-613.

13. R. Karthik and S. Meenakshi, *Int. J.Biol. Macromol.*, 2014, **67**, 210-219.
14. A. Santhana Krishna Kumar, C. Uday Kumar, V. Rajesh and N. Rajesh, *Int. J.Biol. Macromol.*, 2014, **66**, 135-143.
15. L. Zhang, W. Xia, B. Teng, X. Liu and W. Zhang, *Chem. Eng. J.*, 2013, **229**, 1-8.
16. G. Z. Kyzas, M. Kostoglou, N. K. Lazaridis and D. N. Bikiaris, *J. Hazard Mater.*, 2013, **244-245**, 29-38.
17. S. H. Hsu, Y. B. Chang, C. L. Tsai, K. Y. Fu, S. H. Wang and H. J. Tseng, *Colloid. Surface. B*, 2011, **85**, 198-206.
18. A. S. Berezin and Y. A. Skorik, *Carbohyd. Polym.*, 2015, **127**, 309-315.
19. A. Giannakas, K. Grigoriadi, A. Leontiou, N. M. Barkoula and A. Ladavos, *Carbohyd. Polym.*, 2014, **108**, 103-111.
20. M. Yadav, K. Y. Rhee, S. J. Park and D. Hui, Compos. Part B-Eng., 2014, **66**, 89-96.
21. L. Li, L. Fan, M. Sun, H. Qiu, X. Li, H. Duan and C. Luo, *Colloid. Surface. B*, 2013, **107**, 76-83.
22. G. Z. Kyzas, N. A. Travlou and E. A. Deliyanni, *Colloid. Surface. B*, 2014, **113**, 467-476.
23. I. Chowdhury, M. C. Duch, N. D. Mansukhani, M. C. Hersam and D. Bouchard, *Environ. Sci. Technol.*, 2014, **48**, 9382-9390.
24. O. Mabayoje, M. Seredych and T. J. Bandosz, *J. Colloid. Interf. Sci.*, 2012, **378**, 1-9.
25. K. Zhang, V. Dwivedi, C. Chi and J. Wu, *J. Hazard Mater.*, 2010, **182**, 162-168.
26. G. Z. Kyzas, D. N. Bikiaris, M. Seredych, T. J. Bandosz and E. A. Deliyanni, *Bioresource technol.*, 2014, **152**, 399-406.
27. N. A. Travlou, G. Z. Kyzas, N. K. Lazaridis and E. A. Deliyanni, *Chem. Eng. J.*, 2013, **217**, 256-265.
28. L. Fan, M. Li, Z. Lv, M. Sun, C. Luo, F. Lu and H. Qiu, *Colloid. Surface. B*, 2012, **95**, 42-49.
29. L. Fan, Y. Zhang, X. Li, C. Luo, F. Lu and H. Qiu, *Colloid. Surface. B*, 2012, **91**, 250-257.
30. L. Fan, C. Luo, M. Sun, H. Qiu and X. Li, *Colloid. Surface. B*, 2013, **103**, 601-607.
31. J. Zhu, S. Wei, H. Gu, S. B. Rapole, Q. Wang, Z. Luo, N. Haldolaarachchige, D. P. Young and Z. Guo, *Environ. Sci. Technol.*, 2012, **46**, 977-985.
32. I. Larraza, M. López-Gónzalez, T. Corrales and G. Marcelo, *J. Colloid. Interf. Sci.*, 2012, **385**, 24-33.
33. Y. Zhao, J. Li, L. Zhao, S. Zhang, Y. Huang, X. Wu and X. Wang, *Chem. Eng. J.*, 2014, **235**, 275-283.
34. C. Shan, Z. Ma, M. Tong and J. Ni, *Water Res.*, 2015, **69**, 252-260.
35. Y. Zhang, W. Wang, Q. Li, Q. Yang, Y. Li and J. Du, *Talanta*, 2015, **141**, 33-40.
36. M. Esmaeilpour, J. Javidi, F. Dehghani and F. Nowroozi Dodeji, *RSC Adv.*, 2015, **5**, 26625-26633.
37. T. V. Podust, T. V. Kulik, B. B. Palyanytsya, V. M. Gun'ko, A. Tóth, L. Mikhalovska, A. Menyhárd and K. László, *Appl. Surf. Sci.*, 2014, **320**, 563-569.
38. W. Stöber, A. Fink and E. Bohn, *J. Colloid. Interf. Sci.*, 1968, **26**, 62-69.

39. Z. Wu, H. Zhong, X. Yuan, H. Wang, L. Wang, X. Chen, G. Zeng and Y. Wu, *Water Res.*, 2014, **67**, 330-344.
40. N. A. Travlou, G. Z. Kyzas, N. K. Lazaridis and E. A. Deliyanni, *Langmuir*, 2013, **29**, 1657-1668.
41. Y. Ren, H. A. Abbood, F. He, H. Peng and K. Huang, *Chem. Eng. J.*, 2013, **226**, 300-311.
42. N. Ye, Y. Xie, P. Shi, T. Gao and J. Ma, *Mat. Sci. Eng. A-Struct.*, 2014, **45**, 8-14.
43. H. Wang, Y. G. Liu, G. M. Zeng, X. J. Hu, X. Hu, T. T. Li, H. Y. Li, Y. Q. Wang and L. H. Jiang, *Carbohyd. Polym.*, 2014, **113**, 166-173.
44. Y. Li, B. Gao, T. Wu, D. Sun, X. Li, B. Wang and F. Lu, *Water res.*, 2009, **43**, 3067-3075.
45. X. Sun, L. Yang, Q. Li, J. Zhao, X. Li, X. Wang and H. Liu, *Chem. Eng. J.*, 2014, **241**, 175-183.
46. L. Fan, C. Luo, M. Sun and H. Qiu, *J. Mater. Chem.*, 2012, **22**, 24577.
47. T. Wang, L. Zhang, C. Li, W. Yang, T. Song, C. Tang, Y. Meng, S. Dai, H. Wang, L. Chai and J. Luo, *Environ. Sci. Technol.*, 2015, **49**, 5654-5662.
48. X.-j. Hu, Y.-g. Liu, H. Wang, A.-w. Chen, G.-m. Zeng, S.-m. Liu, Y.-m. Guo, X. Hu, T.-t. Li, Y.-q. Wang, L. Zhou and S.-h. Liu, *Sep.Purif. Technol.*, 2013, **108**, 189-195.
49. L. Fan, C. Luo, Z. Lv, F. Lu and H. Qiu, *J. Hazard Mater.*, 2011, **194**, 193-201.

Figure and Scheme captions

Scheme 1. Synthesis of MSCG and the application for removal of Cr(VI) with the help of an external magnetic field

Scheme 2. Proposed mechanism of Cr(VI) removal by MSCG.

Fig. 1. The TEM images of (a) Fe_3O_4, (b) $Fe_3O_4@SiO_2$, (e) GO, (f) MSCG; The SEM images of (c) GO, (d) MSCG.

Fig. 2. XRD patterns of (a) Fe_3O_4, (b) $Fe_3O_4@SiO_2$, (c) MSCG.

Fig. 3. FTIR spectra of (a) Fe_3O_4, (b) $Fe_3O_4@SiO_2$, (c) GO, (d) MSCG.

Fig. 4. XPS spectrum of MSCG : (a) wide scan; (b) C 1s; (c) N 1s; (d) O 1s.

Fig. 5. Magnetization curve of (a) Fe_3O_4, (b) $Fe_3O_4@SiO_2$, (c) MSCG.

Fig. 6 Effect of pH on Cr(VI) adsorption onto Fe_3O_4, $Fe_3O_4@SiO_2$ and MSCG.

Fig.7. Zeta potentials of MSCG at different pH and effect of pH on adsorption of Cr(VI) by MSCG.

Fig.8 (a) Pseudo-secondorder sorption kinetics; (b) Intraparticle diffusion kinetics. (m/V = 0.4 g/L, pH=2±0.1, T = 298 K, t=24 h).

Fig.9. Langmuir and Freundlich non-linear plots of sorption isotherms for Cr(VI) onto MSCG at 298, 308 and 318 K. The dashed lines are Langmuir model simulation, and the solid lines are Freundlich model simulation (m/V = 0.4 g/L, pH=2±0.1, t=24 h)

Fig. 10 The XPS high-resolution spectra of (a) Cr 2p and (b) N 1s.

Fig.11 Reusability of the MSCG for Cr(VI) removal

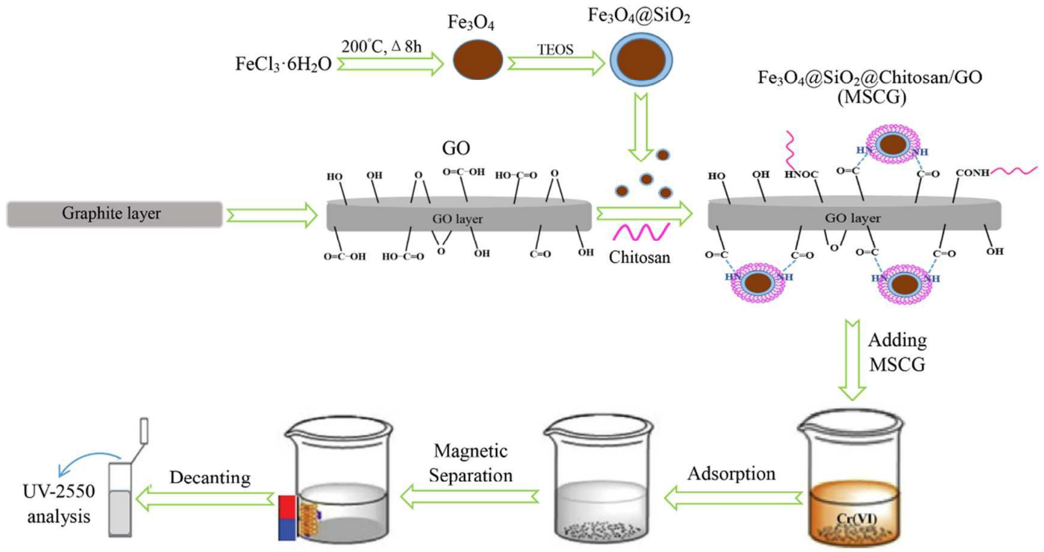

Scheme 1. Synthesis of MSCG and the application for removal of Cr(VI) with the help of an external magnetic field

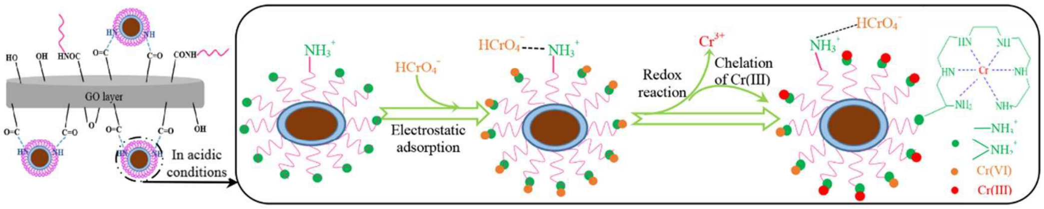

Scheme 2. Proposed mechanism of Cr(VI) removal by MSCG.

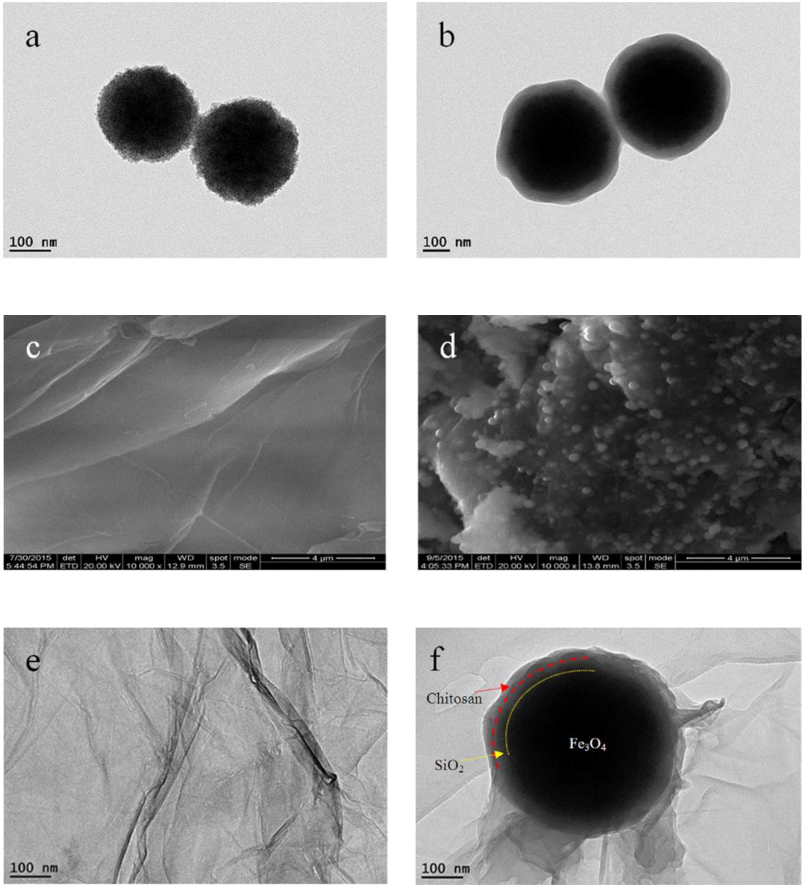

Fig. 1. The TEM images of (a) Fe_3O_4, (b) $Fe_3O_4@SiO_2$, (e) GO, (f) MSCG; The SEM images of (c) GO, (d) MSCG.

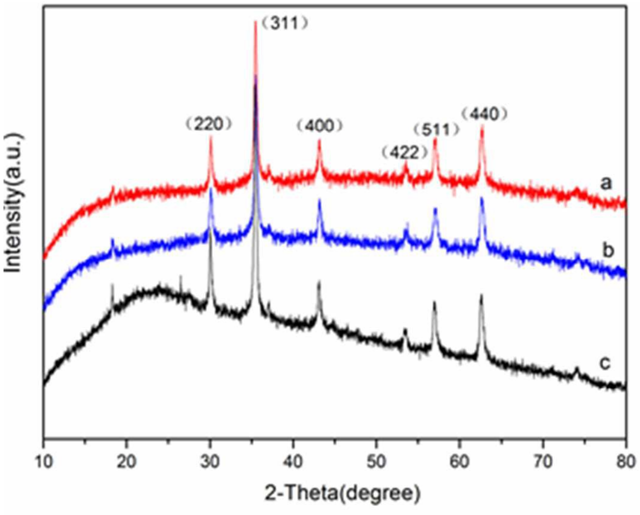

Fig. 2. XRD patterns of (a) Fe_3O_4, (b) Fe_3O_4@SiO_2, (c) MSCG.

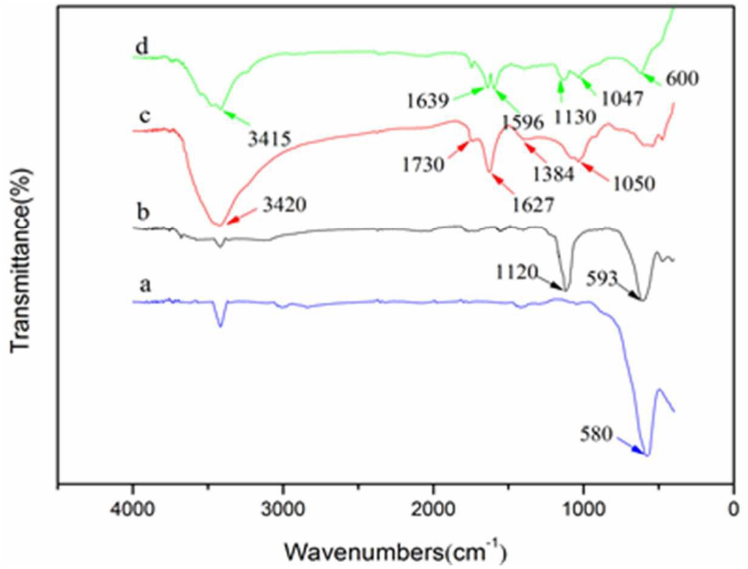

Fig. 3. FTIR spectra of (a) Fe_3O_4, (b) $Fe_3O_4@SiO_2$, (c) GO, (d) MSCG.

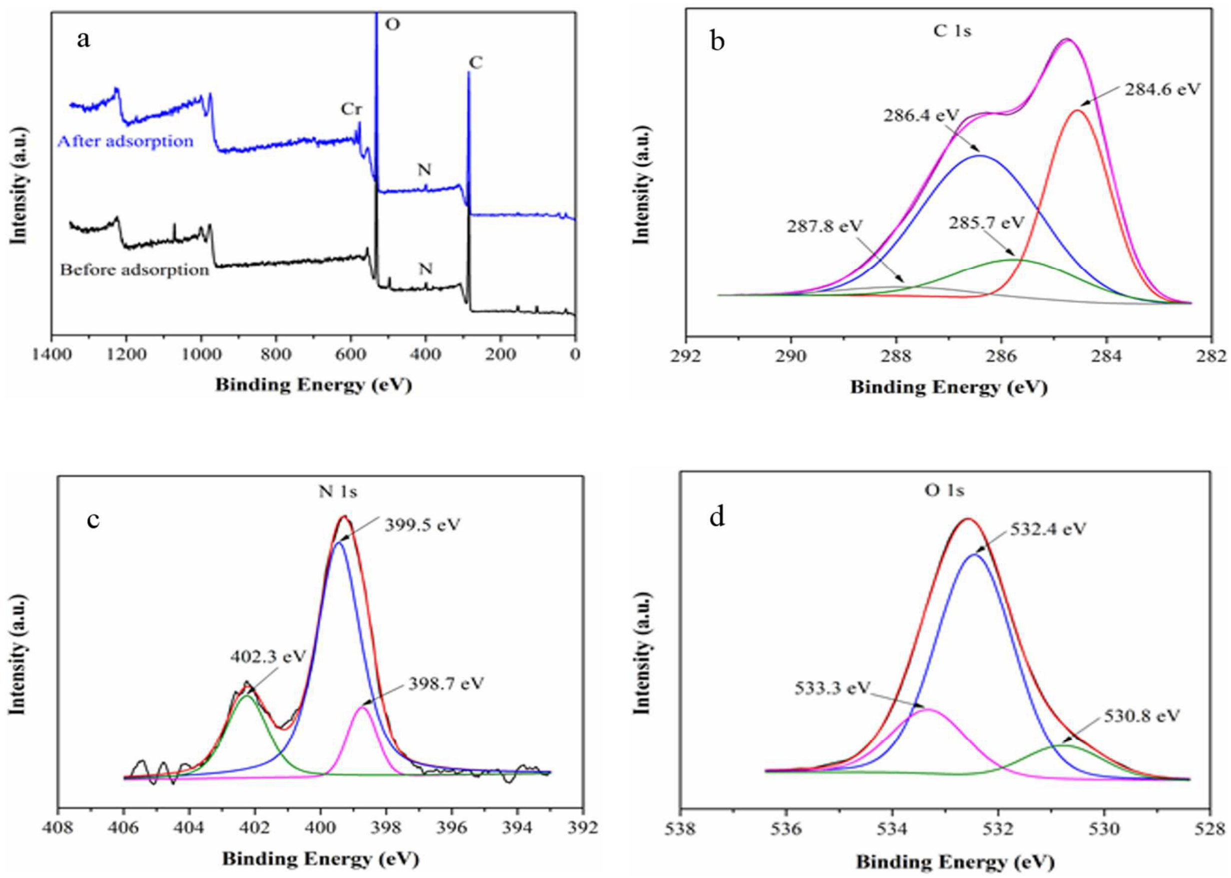

Fig. 4. XPS spectrum of MSCG : (a) wide scan; (b) C 1s; (c) N 1s; (d) O 1s.

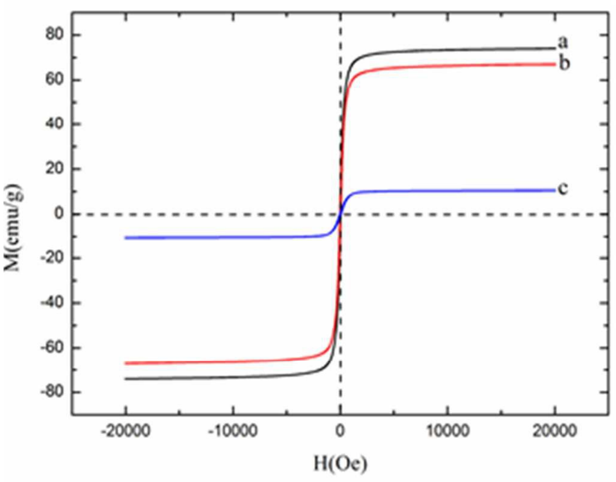

Fig. 5. Magnetization curve of (a) Fe_3O_4, (b) $Fe_3O_4@SiO_2$, (c) MSCG.

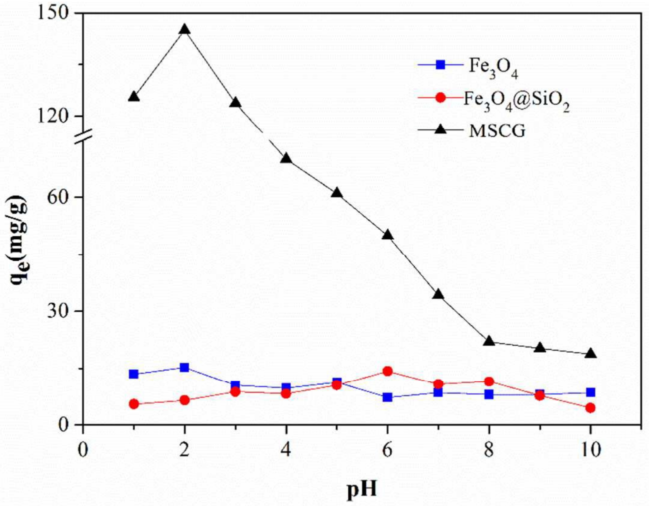

Fig. 6 Effect of pH on Cr(VI) adsorption onto Fe_3O_4, Fe_3O_4@SiO_2 and MSCG.

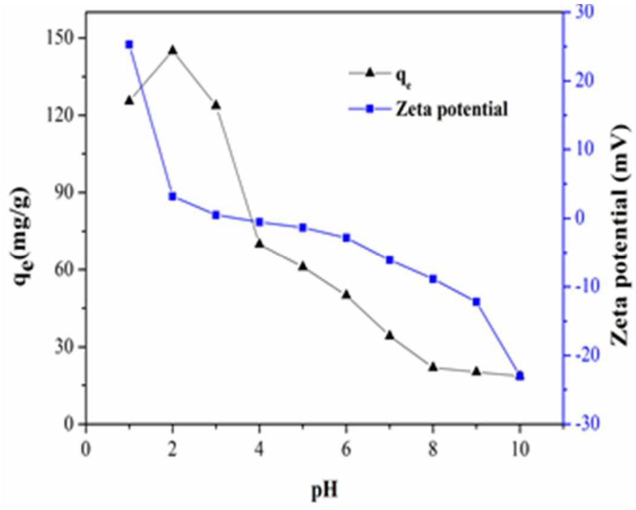

Fig.7. Zeta potentials of MSCG at different pH and effect of pH on adsorption of Cr(VI) by MSCG.

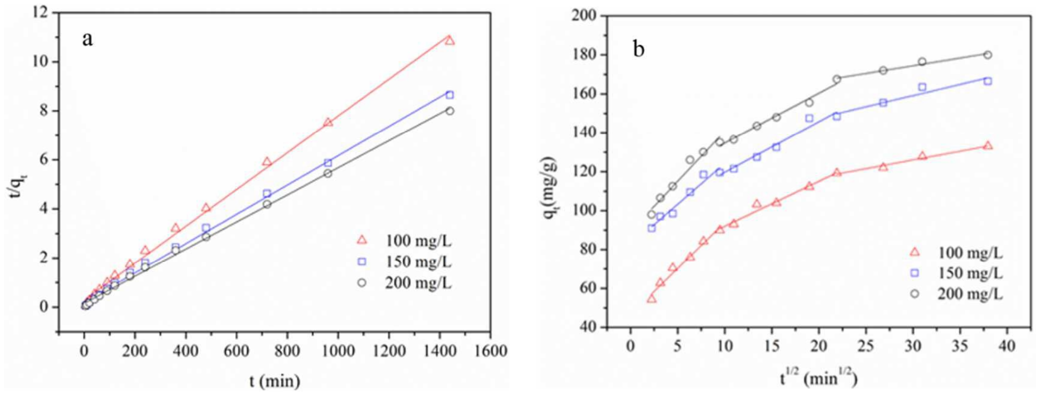

Fig.8 (a) Pseudo-second order sorption kinetics; (b) Intraparticle diffusion kinetics. (m/V = 0.4 g/L, pH=2±0.1, T = 298 K, t=24 h).

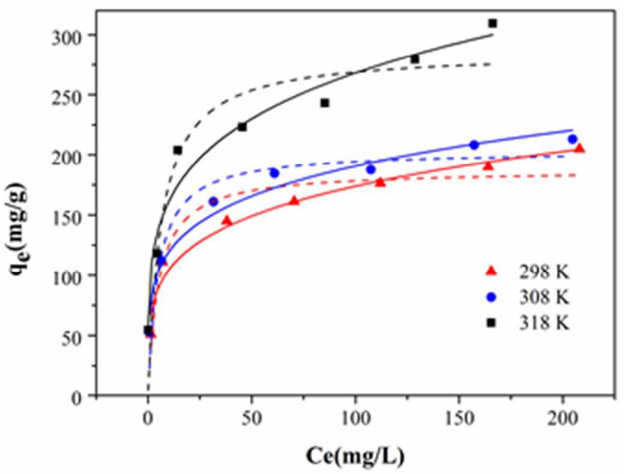

Fig.9. Langmuir and Freundlich non-linear plots of sorption isotherms for Cr(VI) onto MSCG at 298, 308 and 318 K. The dashed lines are Langmuir model simulation, and the solid lines are Freundlich model simulation (m/V = 0.4 g/L, pH=2±0.1, t=24 h)

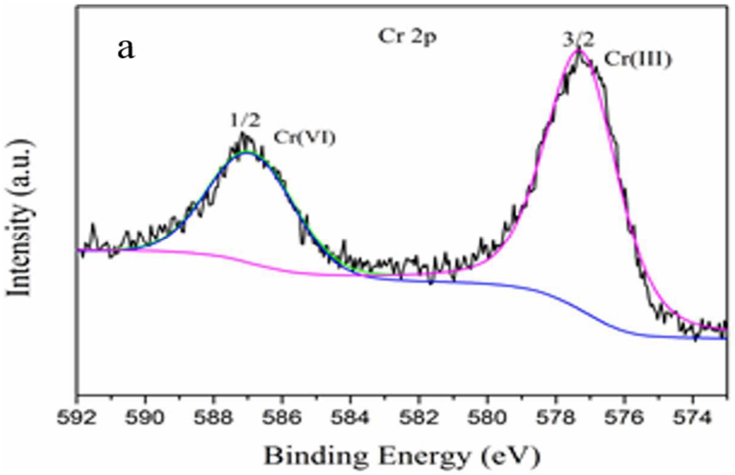

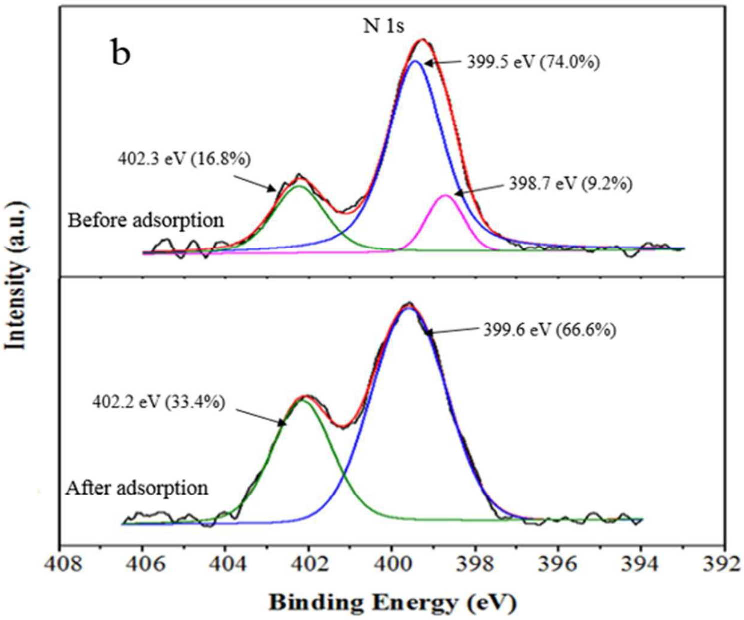

Fig. 10 The XPS high-resolution spectra of (a) Cr 2p and (b) N 1s.

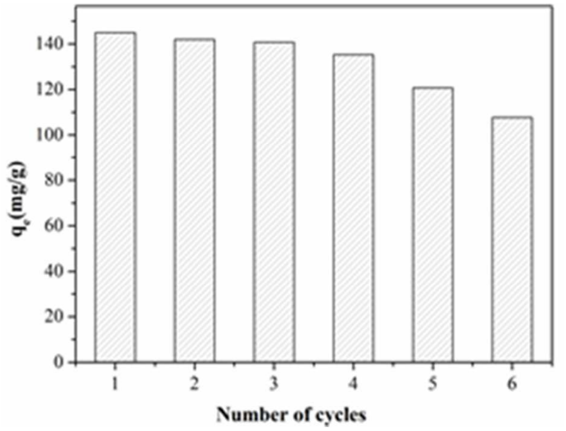

Fig.11 Reusability of the MSCG for Cr(VI) removal.

Tables

Table 1 Kinetic parameters of Cr(VI) sorption on MSCG

Concentration (mg/L)	Pseudo-first-order kinetic				Pseudo-second-order kinetic			
	$q_{e,exp}$ (mg/g)	K_1 (1/min)	$q_{e,cal}$ (mg/g)	R^2	$q_{e,exp}$ (mg/g)	K_2 (g/mg.min)	$q_{e,cal}$ (mg/g)	R^2
100	133	2.63×10^{-3}	60.059	0.957	133	1.88×10^{-4}	133.51	0.997
150	166.5	3.00×10^{-3}	67.301	0.969	166.5	1.77×10^{-4}	167.50	0.997
200	180	3.10×10^{-3}	67.104	0.983	180	1.89×10^{-4}	181.16	0.998

Table 2 Intra-particle diffusion parameters for different initial Cr(VI)concentrations

C_o(mg/L)	K_{1d} (mg/g.min$^{1/2}$)	K_{2d} (mg/g.min$^{1/2}$)	K_{3d} (mg/g.min$^{1/2}$)	C_1	C_2	C_3	$(R_1)^2$	$(R_2)^2$	$(R_3)^2$
100	4.728	2.310	0.893	46.620	68.885	99.230	0.970	0.971	0.968
150	4.195	2.724	1.041	82.293	92.200	128.385	0.947	0.967	0.895
200	5.137	2.565	0.789	89.380	109.092	150.794	0.957	0.977	0.958

Table 3 Isotherm parameters for the adsorption of Cr(VI) onto MSCG

Isotherms	Parameters	Temperature (K)		
		298	308	318
Langmuir	$q_{\max}$ (mg/g)	187.262	203.489	285.858
	K_L (L/mg)	0.198	0.210	0.158
	R^2	0.909	0.906	0.875
Freundich	$1/n$	0.222	0.203	0.221
	K_F (L/mg)	62.622	74.775	96.797
	R^2	0.962	0.967	0.964

Table 4 Thermodynamic parameters for Cr(VI)adsorption on MSCG

T(K)	ΔG°(kJ/mol)	ΔH°(J/(K mol))	ΔS°(kJ/mol)
298	-20.34	40.77	204.30
308	-21.69		
318	-24.43		